Article

# Novel Study of Strain-Induced Piezoelectricity in VO₂

Raktima Basu,* Geramilla Mangamma,* and Sandip Dhara

Read Online

ACCESS | 📊 Metrics & More | 📖 Article Recommendations | 🔵SI Supporting Information

**ABSTRACT:** VO₂ is well known for its dual-phase transitions, electrical and structural, at a single temperature of 340 K. The low-temperature structural phases of VO₂ are different from their high-temperature counterpart in terms of structural symmetry. The strain-induced modification of the structural distortion in VO₂ is studied in detail. A ferroelectric-type distortion is observed, and therefore, the piezoelectric effect in the low-temperature phases of VO₂ is investigated, for the first time, by piezoresponse force microscopy. Strain is one of the factors that can modify the electronic behavior of piezoelectric materials. At the same time, the two low-temperature phases of VO₂ (M1 and M2) can only be separated by the application of strain. The piezoelectric coefficient in the strained phase of VO₂ was found to be 11−12 pm/V, making it eligible for piezotronic applications.
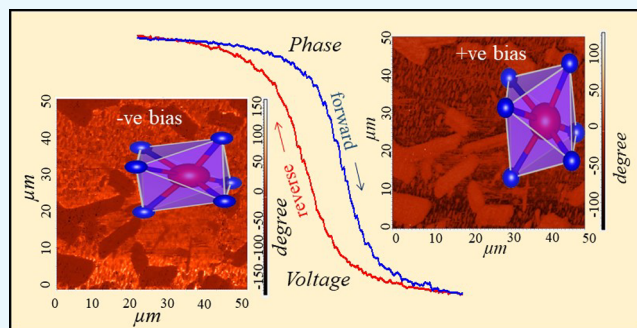
## INTRODUCTION

Piezoelectric materials have attracted attention in recent times because of their fruitful applications in renewable energy production, such as self-powered devices, microactuators, pressure sensors, ultrasonic motors, and mechanical energy harvesting, among others.[1−5] Piezoelectricity is nothing but the production of electrical potential inside a noncentrosymmetric material subjected to a mechanical strain or vice versa. Therefore, all ferroelectric materials exhibit a piezoelectric effect due to a lack of symmetry. Among vanadium oxides, V₂O₅ is a ferroelectric material with a Curie temperature of 530 K.[6] The piezoelectricity, and thus ferroelectricity, in VO₂ has not been investigated so far, although it has been predicted in previous reports.[7] However, VO₂ draws significant attention for its well-known metal-to-insulator transition (MIT) near room temperature (340 K).[8] VO₂ crystallizes in monoclinic, M1 ($P2_1/c$), and rutile tetragonal, R ($P4_2/mnm$), structures below and above the transition temperature, respectively.[9,10] V atoms are symmetrically spaced along the $c_R$ axis in the high-temperature R phase, with lattice parameters $a_R = b_R = 4.55$ Å and $c_R = 2.85$ Å (Figure 1a).[11] Each V atom in the R phase is surrounded by a regular oxygen octahedron. However, the volume of the unit cell becomes double in the low-temperature M1 phase with new lattice parameters $a_{M1} = 5.70$ Å, $b_{M1} = 4.55$ Å, $c_{M1} = 5.38$ Å, and $\beta_{M1} = 123°$.[12] The change in lattice parameters brings significant differences in the arrangement of V atoms along the $c_R$ axis. The V atoms form pairs, and the pairs tilt along the $c_R$ axis, which leads the vanadium ion to move away from the center of the oxide octahedron (Figure 1b). The deformation of the octahedron changes the identical V−O bonds of the R phase to different long and short V−O bonds.[13] Moreover, another monoclinic phase of VO₂, M2
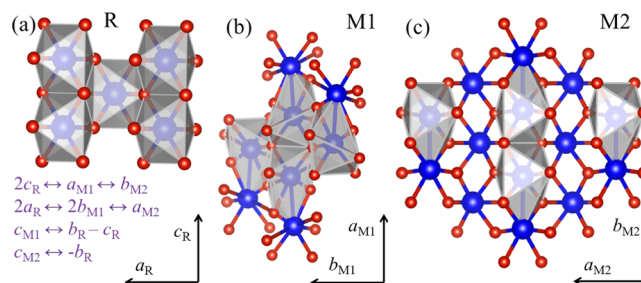


**Figure 1.** Schematic structures for (a) rutile tetragonal R, (b) monoclinic, M1, and (c) monoclinic, M2 phases of VO₂. Large (blue) and small (red) balls denote V and O atoms, respectively.

($C2/m$), is also reported to evolve during the phase transition from M1 to R.[14] The metastable M2 phase of VO₂ is reported to be stabilized at room temperature by introducing strain in the system, either via mechanical strain or via doping with metals of lower valency than V⁴⁺ (e.g., Al³⁺, Ga³⁺, Cr³⁺).[15,16] For the M2 phase, in one of the sublattices, the V ions along the $c_R$ axis dimerize without twisting, while the V ions in the nearest sublattice remain nondimerized and form canted V−V chains (Figure 1c). Due to different arrangements of V atoms in subsequent sublattices, the oxide octahedra deform from their regular shape as in the R phase. The lattice parameters for
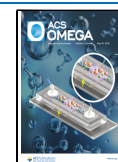
the M2 phase are $a_{M2}$ = 9.07 Å, $b_{M2}$ = 5.797 Å, $c_{M2}$ = 4.53 Å, and $\beta_{M2}$ = 91.88°.[17]

In both low-temperature phases of $VO_2$, the tilting of the $c_R$-axis (in one sublattice for M2) shortens the V–O separation perpendicular to the $c_R$-axis.[14] The relocation of a cation from the center of the octahedra toward one or more anions results in a ferroelectric-type distortion. The dielectric constant of $VO_2$ is also reported to be low ($\sim$40)[18] and so is of special interest for the piezoelectric effect. Strain is one of the factors that can modify the electronic behavior of piezoelectric materials. Concurrently, the two low-temperature phases (M1 and M2) in the phase diagram of $VO_2$ can only be separated by the application of strain.[19,20] In the present report, therefore, we have studied the piezoelectric effect in both M1 and M2 phases of $VO_2$, for the first time, by piezoresponse force microscopy (PFM).

## ■ EXPERIMENTAL DETAILS

The samples of $VO_2$ were grown on a Si(111) substrate using the chemical vapor transport method at 1150 K for 3 h with Ar as the carrier gas. Two types of samples were synthesized: sample S1, for which only pure $VO_2$ powder (Sigma-Aldrich, 99%) was placed in a high-purity alumina boat, which, in turn, was kept inside a sealed quartz tube, and sample S2, for which Mg powder was kept along with $VO_2$ for doping. Morphological analysis of the pristine samples was studied using a field emission scanning electron microscope (FESEM, SUPRA 55 Zeiss). The structural properties of the samples were studied by X-ray diffraction ($\lambda$ = 0.76089 Å) at beamline 11 of Indus-2 synchrotron facility, India, using a Si(111) channel-cut monochromator. We have used FIT2D software[21] for the calibration and conversion of 2-D diffraction data to 1-D, intensity vs $2\theta$ profile. Rietveld refinement was subsequently carried out using GSAS + EXPGUI software.[22] Visualization of the crystal structure and calculation of the bond lengths after Rietveld refinement were performed using VESTA[23] software. Raman spectra of the as-grown samples were recorded using a Micro-Raman spectrometer (inVia, Renishaw, U.K.) operating in the backscattering configuration with an Ar+ laser (514.5 nm) as an excitation source, a diffraction grating of 1800 g/mm as a monochromator and a thermoelectrically cooled CCD camera as the detector. The piezoelectric response of the samples was studied using an NT-MDT, NTEGRA scanning probe microscope. A conductive tip (diamond-like carbon-coated) was used in a contact mode configuration to study the piezoelectric as well as ferroelectric properties of the studied samples. In this experiment, a DC bias induces a polarization in the sample and an AC bias (amplitude 0.3 V and frequency 255 kHz) helps in measuring the piezoelectric response. A lock-in amplifier helps in measuring the amplitude and phase information and generates the corresponding images over a predefined raster-scanned area of the sample. In the PFM output, we focus on two parameters: (i) the amplitude, which imitates the weight of the piezoresponse and (ii) the phase, which reflects the polarization direction of the sample. We have experimented with the DC bias ranging from −10 to +10 V. The value of $V_{dc}$ was set to 0, and $V_{ac}$ was kept minimum while measuring the $d_{33}$ value to reduce the contribution from the electrostatic term (explained in detail in the next section).

## ■ RESULTS AND DISCUSSION

The FESEM images of the pristine samples are shown in Figure 2. The as-grown microcrystals have an average width of
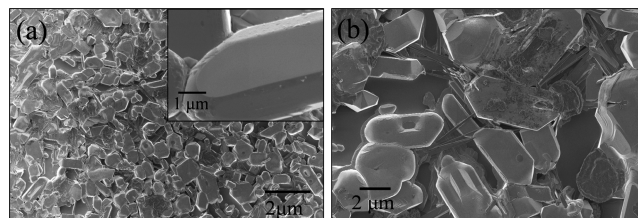


**Figure 2.** FESEM images of as-grown microcrystals for (a) sample S1 and micro- and nanocrystals for (b) sample S2. The inset of (a) shows a magnified image of a single microrod.

2−5 $\mu$m for sample S1 (Figure 2a). The inset of Figure 2a shows a magnified image of a single crystal microrod of width $\sim$2 ± 0.5 $\mu$m. However, in the case of sample S2 (Figure 2b), both micro and nanorods were observed to be present. The average width of microrods was 2−6 $\mu$m, and that for nanorods was $\sim$200 ± 40 nm for sample S2. The (011) plane of the monoclinic M1 phase is the preferential growth plane for $VO_2$. Our earlier HRTEM studies (also described in Figure S2) for a single crystal $VO_2$ showed the sample in the (011) orientation and growth axis along the $[100]_{M1}$.[24]

We carried out glancing incidence x-ray diffraction (GIXRD; Bruker D8) for the pristine samples S1 and S2 on a Si substrate using a Cu K$\alpha$ radiation source of wavelength, $\lambda$ = 1.5406 Å (Figure S1). However, to confirm the pure phases and calculate the bond-lengths, we took out a few microcrystals and ground them to carry out XRD studies using the synchrotron facility. The Rietveld refined X-ray crystallographic patterns are shown in Figure 3a,b. In sample S1 (Figure 3a), the diffraction peaks reflect the M1 phase of $VO_2$ (JCPDS No. 04-007-1466)[25] with $R_{WP}$ = 0.056 and $R_p$ = 0.043. However, for sample S2 (Figure 3b), the diffraction peaks confirm the presence of the M2 phase of $VO_2$ (JCPDS No. 01-071-0289)[26] with $R_{WP}$ = 0.048 and $R_p$ = 0.036. At lower $2\theta$ values, the diffraction peak at a $2\theta$ value of 13.67° represents the (011) plane corresponding to the M1 phase (equivalent to the $(110)_R$ plane) of $VO_2$ for samples S1. However, in the case of sample S2, the peak splits into two diffraction peaks and is observed at $2\theta$ values of 13.38 and 13.84° corresponding to the ($\bar{2}$01) and (201) planes of the M2 phase of $VO_2$.[27]

The M2 phase is reported to be the strained version of the M1 phase.[17,19] However, in our study, the contribution of the substrate in inducing strain in these samples can be ignored as both samples were synthesized on the same substrate. We found that Mg as a dopant introduces strain in the sample, stabilizing the metastable M2 phase in sample S2. The role of the Mg dopant in replacing $V^{4+}$ with $V^{5+}$ and stabilizing the other metastable phases of $VO_2$ is studied by X-ray photoelectron spectroscopy (XPS) analyses, and is discussed in detail in the Supporting Information (Figure S3). The lattice parameter $b_{M2} > a_{M1}$ (equivalent to $c_R$) indicates a tensile strain along the $c_R$ axis, which is responsible for stabilizing the M2 phase. The detailed analysis is reported in our previous studies.[28,29] We calculated the tensile strain along the $c_R$ axis, which is found to be $\sim$8.2 × $10^{-3}$.

Using VESTA software, we calculated the V–V and V–O bond lengths after Rietveld refinement. The V–V lengths were
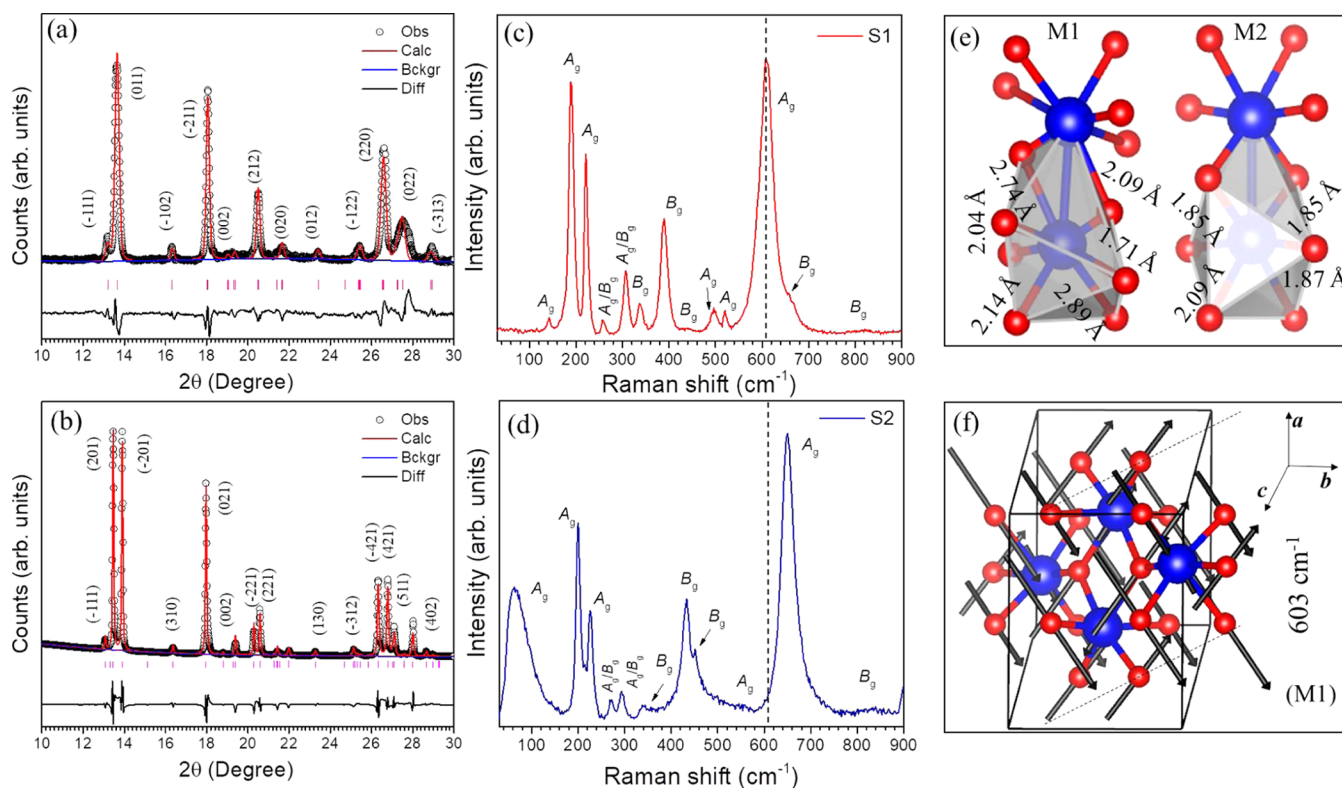
**Figure 3.** Rietveld fitted diffraction pattern for samples (a) S1 and (b) S2. Raman spectra with proper symmetry notations of the pristine samples (c) S1 and (d) S2. Dashed lines are a guide to the eye. (e) Schematics of V−O bond lengths of M1 and M2 calculated using VESTA, and (f) schematic atomic displacement for the 603 cm$^{-1}$ phonon mode of the M1 phase. The V and O atoms are shown as large (blue) and small (red) balls, respectively, and the directions of the displacements of atoms are represented as arrows.

2.60 Å (intradimer) and 3.11 Å (interdimer) along the $c_R$ axis. However, in the case of the M2 phase, V−V separations were found to be 2.51 Å (intradimer) and 3.26 Å (inter-dimer) for the dimerized V-chains along the $c_R$ axis. However, for the nondimerized zig-zag V-chains, all V−V bonds were found to have a single length of 2.95 Å. The observed bond lengths are almost similar as reported earlier.[7,30] The V−O distances in the deformed octahedron were found to be 2.89 and 2.74 (bridging oxygens between paired vanadium ions), 2.04 and 2.09 (connecting oxygens between two V-chains), and 2.14 and 1.71 Å (Figure 3e) for the M1 phase. However, for the M2 phase (Figure 3e), the V−O separations between the V-chains, i.e., perpendicular to the (011) plane, were found to be shortened (1.85 and 1.87 Å). The tensile strain along the $c_R$ axis may lead to compression in its perpendicular direction. The other pairs of V−O bond length were found to be 2.09 Å.

The spectroscopic investigations were performed to fetch additional information about the phase-purity along with the strain present in the as-grown samples. The Raman spectra collected from both samples at room temperature are portrayed in Figure 3c,d. Group theory calculations predict 18 Raman mode frequencies for both M1 and M2 phases of VO$_2$. However, for the M1 phase, the mode symmetries are $9A_g + 9B_g$, whereas for the M2 phase $10A_g + 8B_g$, at the Γ point.[31,32]

However, we observed 12 Raman mode frequencies for samples S1 (Figure 3c) at 142, 189(A$_g$), 224(A$_g$), 257(either A$_g$ or B$_g$; A$_g$/B$_g$), 306(A$_g$/B$_g$), 335(A$_g$), 389(A$_g$/B$_g$), 439(A$_g$/B$_g$), 496(A$_g$/B$_g$), 609(A$_g$), 664(B$_g$), and 823(B$_g$) cm$^{-1}$, confirming the presence of a pure M1 phase of VO$_2$.[33,34] However, for samples S2, 11 Raman modes at ∼51, 203(A$_g$),

216(A$_g$), 229(A$_g$), 273(A$_g$/B$_g$), 296(A$_g$), 341(A$_g$), 431(A$_g$/B$_g$), 455(A$_g$/B$_g$), 651(A$_g$), and 831(B$_g$) cm$^{-1}$ (Figure 3d) were collected, which precisely resembled the M2 phase of VO$_2$.[15,35]

The Raman mode frequency, detected at 609 cm$^{-1}$ in sample S1, is reported to be originated because of V−O bond stretching.[32] We have calculated the phonon density of states for the sample using density functional theory (DFT). The detail of the study is published in one of our previous works.[24] We observed phonon mode at 609 cm$^{-1}$, corresponding to the calculated mode at 603 cm$^{-1}$, as shown schematically in Figure 3f, for the atomic displacements. The V−O vibrations perpendicular to the (011) plane contribute the maximum to the vibrational mode at 609 cm$^{-1}$, which shifts to 651 cm$^{-1}$ in sample S2 (as specified by the dotted line in Figure 3c,d). The blue shift of the Raman mode indicates that the V−O bond length shortens with Mg doping. In pure VO$_2$, the center of the octahedron constitutes a V$^{4+}$ cation, the vertices constitute oxygen anions, and the principal axis is perpendicular to the (011)$_{M1}$ lattice plane.[16] In each octahedron, the central V atom shared its electrons with the neighboring O atoms situated at the vertices. Correspondingly, the O atoms pull the required electrons from three adjacent V atoms. However, after the Mg$^{2+}$ ion replaces the native V$^{4+}$ (d$^1$), the adjacent V$^{4+}$ (d$^1$) sites in the neighboring chains get occupied by V$^{5+}$ (d$^0$) sites.[29,36] The substitution of V$^{4+}$ by V$^{5+}$ results in moving the two apical O$^{2-}$ of the octahedron nearer to one other. As a consequence, the length of V−O bonds decreases,[37] what we observed in the XRD analysis. Figure 3e shows that the oxide-octahedra in both M1 and M2 phases got distorted and became asymmetric due to the off-center displacement of the central V ion. The asymmetry gives rise to a resultant dipole to
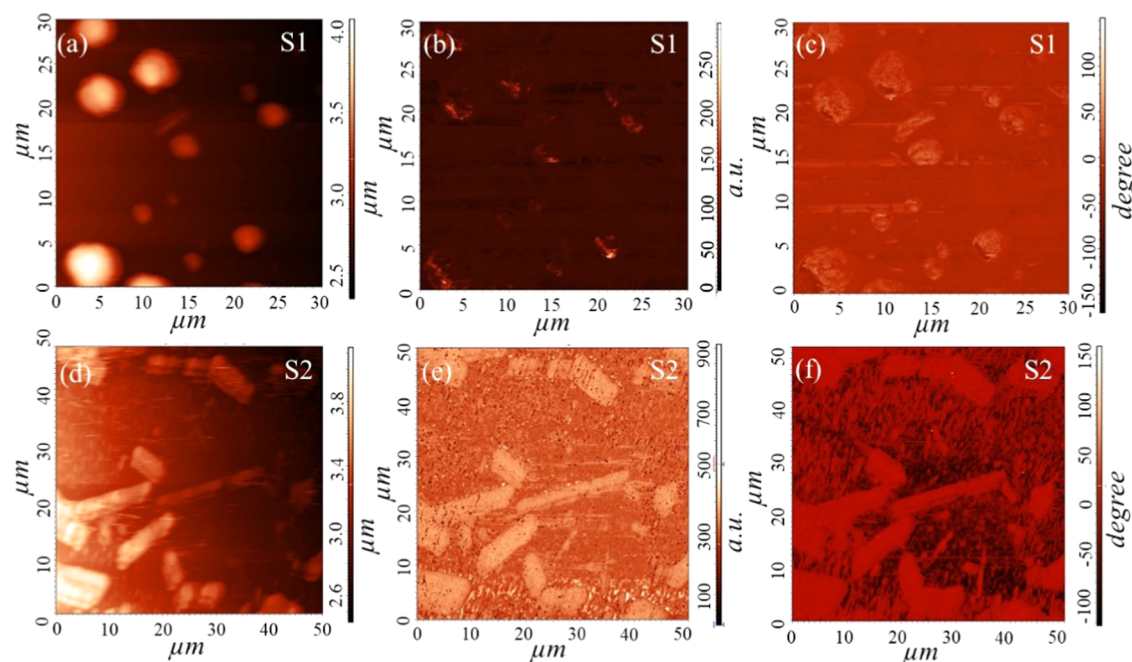
**Figure 4.** (a) Topographic, (b) amplitude, and (c) phase images of sample S1. Corresponding (d) topography, (e) amplitude, and (f) phase images of sample S2.
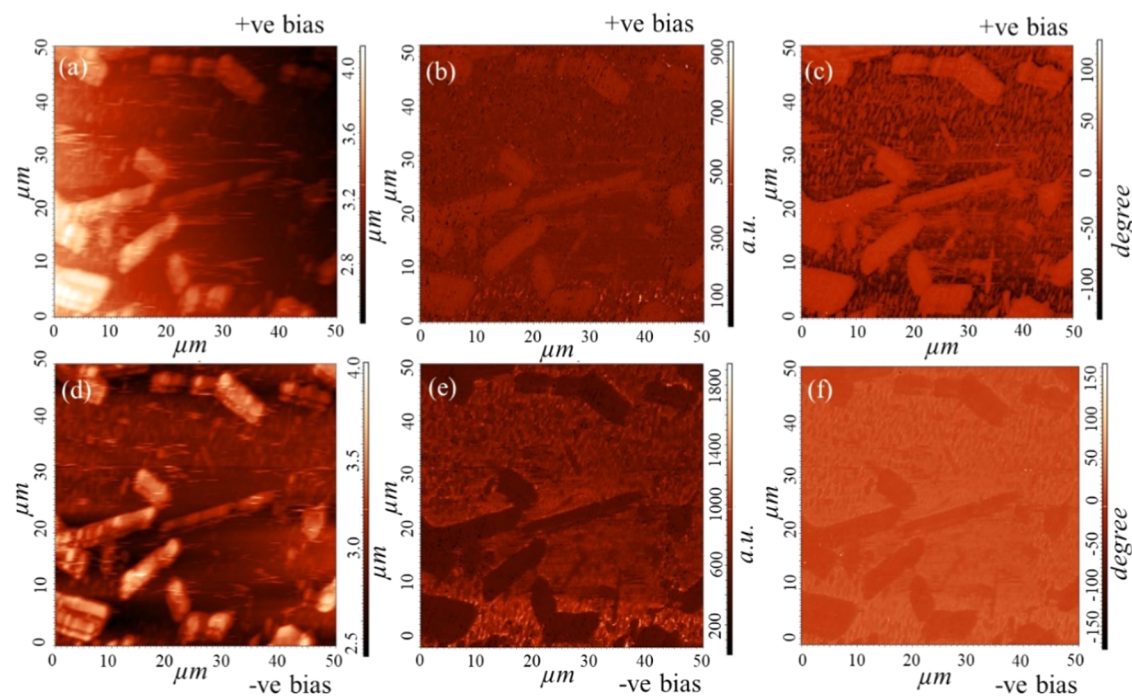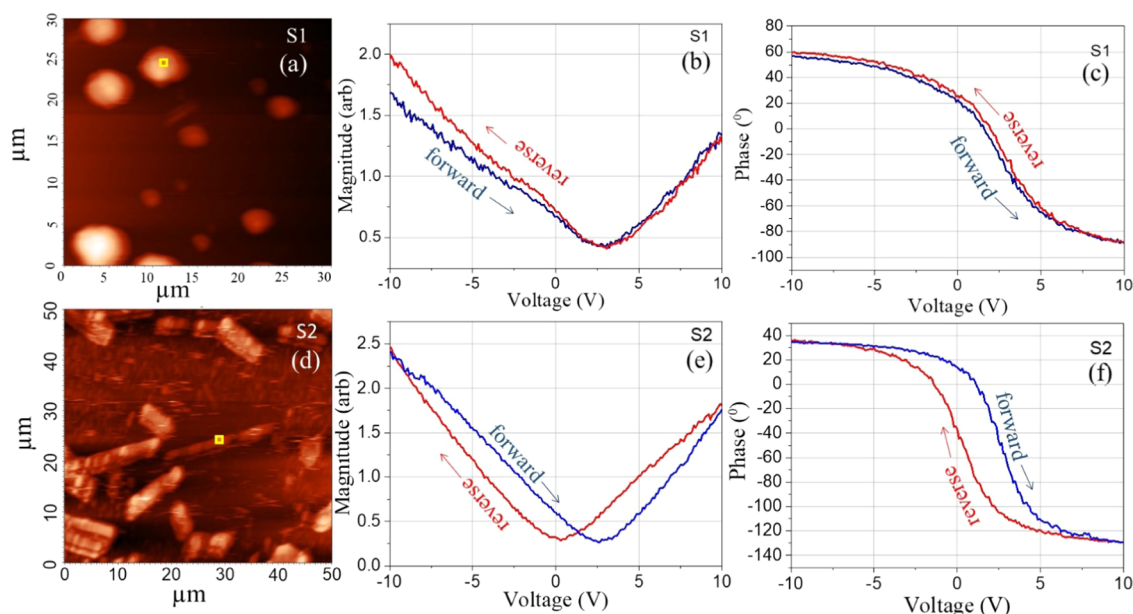


**Figure 5.** (a) Topographic, (b) amplitude, and (c) phase images of sample S2 at +3 V. Corresponding (d) topography, (e) amplitude, and (f) phase images at −3 V.

the crystals along the principal axes of the octahedra (perpendicular to the $(011)_{M1}$ plane). As the structures of both samples show ferroelectric-type distortion, we have carried out the piezoelectric studies on both the samples.

The piezoresponse images were collected after the application of both AC and DC voltages between the sample and the tip. We collected several piezoresponse images at different areas with a scan range of $50 \times 50\ \mu m^2$, among which a few typical topography, amplitude, and phase images are presented in Figure 4a−c for sample S1 and Figure 4d−f for

sample S2. In the topographic image of S1 (Figure 4a), the microcrystals of sizes 2−5 were observed to be distributed over the area. In sample S2, microcrystals and nanocrystals (Figure 4b) were observed as shown in FESEM images (Figure 2).

The amplitude and phase images of sample S1 do not depict significant contrast with respect to the background, signifying negligible piezoresponse for sample S1 (Figure 4b,c). However, in the case of sample S2, the amplitude and phase images (Figure 4e,f) depict bright contrast compared to the substrate implying a higher piezoelectric deformation. The

**Figure 6.** (a) Topography, change in (b) amplitude, and (c) phase of sample S1 for the voltage range −10 to +10 V. Corresponding (d) topography, change in (e) amplitude, and (f) phase of sample S2 for the voltage range −10 to +10 V. The amplitude and phase data were collected from the area marked by a yellow square in the topographic images.

bright contrast also represents that the polarization direction (P) and the applied field (E) are parallel (P∥E) to each other.

As the samples are oriented by the $(011)_{M1}$ face, the electric field direction and the principal axis of the octrahedra are parallel, resulting in bright contrast in piezoresponse imaging.

The electronic behavior of $VO_2$ is reported to be tuned with the application of strain, which is also true for piezoelectric materials. The M2 phase is confirmed as the strained version of the M1 phase of $VO_2$. The cation−anion (V−O) distance along the polar direction is also reduced in the M2 phase. The weak piezoresponse in the M1 phase might be modified with the induced strain, with the M2 phase being ferroelectric.

We carried out PFM studies on considerable sets of alternative bias voltages. The change in amplitude and phase with bias voltage for both samples are shown in Figures S4 and S5. Figure 5 shows a typical piezoresponse (amplitude and phase) along with topography images collected at a bias of +3 and −3 V for sample S2. While applying a +ve bias, the phase image (Figure 5c) shows a bright contrast with respect to the substrate, whereas, upon application of a −ve bias, the sample shows a dark contrast (Figure 5f) with respect to the substrate, indicating the piezoelectric nature of the sample.

Further, to support our claim, we have collected the PFM responses from samples S1 and S2 (M1 and M2 phase of $VO_2$, respectively) for the entire voltage range of −10 to +10 V in both forward and reverse biases. The topography images are also shown in Figure 6 along with the change in amplitude and phase over the voltage range.

We observed that the piezoresponse grows with the upsurge in the voltage for both samples at both forward and reverse sweeps. Sample S1 does not show any hysteresis loop both in magnitude (Figure 6b) and phase (Figure 6c) cycle over the entire voltage range, suggesting the sample to be a nonferro-electric. However, in sample S2, we observe hysteresis for both the magnitude and phase cycles with the switch in voltage bias (Figure 5e,f), confirming that $VO_2$ in its M2 phase is ferroelectric. The hysteresis also indicates that the detected piezoresponse is the cumulative effects of the induced and

spontaneous polarization due to the structural deformation. However, we have also carried out the PFM images at different bias voltages and back to 0 V bias to check the spontaneous polarization. The images are shown in Figure S6.

The hysteresis curves (magnitude and phase loops) for sample S2 show a perfect shape apart from 2 to 2.5 V shift with complete saturation signifying no leakage current, which makes it applicable as a functional device. A similar voltage shift was observed for sample S1 as well. The shift of local PFM hysteresis loops from origin may be due to the presence of a biased-voltage generated between different contacts of the sample with the bottom and top electrodes.[38]

For a material to be ferroelectric, its structures should be such that the correlation of the distortions of neighboring octahedra to afford a resultant dipole to the crystal.[7] In the case of the M1 phase, although the oxide octahedron is asymmetric enough, along the polar direction, the net dipole moment is zero due to antiferroelectric-type distortion (Figure 1b). However, in the case of the M2 phase, due to induced strain, the atomic distribution of V along the $c_R$ axis is different in two sublattices (Figure 1c). Two different types of distortion in the neighboring V chains give rise to a net dipole moment along the polar plane, making the M2 phase ferroelectric.

To evaluate the observed piezoresponse, we have used point spectroscopy and calculated the $d_{33}$ value at $V_{dc} = 0$ V. In PFM, when we apply any modulation voltage V between the piezoelectric material and the tip, we expect a vertical shift of the tip following the piezoelectric movement of the sample, as the sample is in mechanical contact with the tip. The amount of the tip displacement provides information about the piezoelectric strain. Consider that the voltage V is applied to a microcrystal with height h. If the produced electric field $E_3$ (along the c-axis) stretches or shrinks the crystal by an amount $\Delta h$, then the variation of strain along that axis is $\Delta S_3 = \Delta h/h$. The piezoelectric coefficient $d_{33}$ can be written as[39]

$$\text{eff. } d_{33} = \Delta S_3/E_3 \tag{1}$$

where $E_3 = V/h$.

Substituting the values of $\Delta S_3$ and $E_3$ in eq 1, we found effective $d_{33}$ as

$$\text{eff. } d_{33} = \Delta h/V \tag{2}$$

Thus, the piezoelectric coefficient, $d_{33}$, can be easily computed using eq 2 just by dividing the piezoelectric deformation with the subsequently applied AC bias. In our study, the deformation value was determined in pA. However, the output value in pA was converted to an equivalent value in pm using a force−distance curve. We have calculated the value of the eff. $d_{33}$ from various micro- and nanocrystals, and the average value was found to be 11−12 pm/V (with <10% error). The value of eff. $d_{33}$ is quite good in comparison to other semiconducting piezomaterials such as ZnO,[40] ZnS,[41] and III−V nitrides.[42−44] High performance of these oriented micro- and nanocrystals make them useful for many applications like motion sensors, chemical sensors, strain sensors/field sensors, etc. Our study confirms $VO_2$, which is well known for its electronic and optoelectronic properties, is also a suitable piezo-material in its M2 phase, for the first time, making it eligible for piezotronic applications.

## CONCLUSIONS

The $VO_2$ micro- and nanocrystals, in two different structural phases (M1 and M2), are synthesized by the vapor transport technique. The M2 phase was found to be stabilized by the introduction of strain via Mg doping. The piezoresponse force microscopy imaging was carried out systematically on both pristine phases. The $VO_2$ micro- and nanocrystals, stabilized in the M2 phase, showed strong spontaneous polarization w.r.t bias as the main reason for the piezoresponse (i.e., presence of polarization/domain switching w.r.t bias), whereas the $VO_2$ microcrystals grown in the M1 phase, show a very weak piezoresponse w.r.t the applied field (as indicated by a small variation in the phase signal/small variation in the brightness of phase image w.r.t bias—i.e., absence of polarization/domain switching w.r.t bias). So, the induced strain in the M2 phase is anticipated as the main reason for the ferroelectricity or piezoresponse. The M2 phase was also explored as ferroelectric, for the first time, due to the presence of net dipole moment in the neighboring distorted octahedra and polarization along the probed direction. The piezoelectric coefficient, $d_{33} \sim 11-12$ pm/V for the M2 phase of $VO_2$ was calculated using the PFM technique, which is quite good compared to other semiconducting piezomaterials. The current work provides insight into $VO_2$, which is well known for its electronic and optoelectronic properties, and is also eligible for piezotronic applications.

## ASSOCIATED CONTENT

### SI Supporting Information

The Supporting Information is available free of charge at https://pubs.acs.org/doi/10.1021/acsomega.2c00645.

GIXRD pattern and TEM images of the two phases of $VO_2$ with preferred orientation and growth direction, XPS spectra for the atomic percentage of the elements present, and the piezoelectric topography, amplitude, and phase images of both the phases of $VO_2$ at various bias voltages (PDF)

## AUTHOR INFORMATION

### Corresponding Authors

**Raktima Basu** − *Surface and Nanoscience Division, Indira Gandhi Centre for Atomic Research, A CI of Homi Bhabha National Institute, Kalpakkam 603102, India*; Present Address: Department of Physical Sciences, Indian Institute of Science Education and Research, Kolkata, Mohanpur Campus, Mohanpur 741246, Nadia, West Bengal, India; orcid.org/0000-0003-1545-8957; Email: raktimabasu14@gmail.com

**Geramilla Mangamma** − *Surface and Nanoscience Division, Indira Gandhi Centre for Atomic Research, A CI of Homi Bhabha National Institute, Kalpakkam 603102, India*; Email: gm@igcar.gov.in

### Author

**Sandip Dhara** − *Surface and Nanoscience Division, Indira Gandhi Centre for Atomic Research, A CI of Homi Bhabha National Institute, Kalpakkam 603102, India*; orcid.org/0000-0001-9728-9952

Complete contact information is available at:
https://pubs.acs.org/10.1021/acsomega.2c00645

### Notes

The authors declare no competing financial interest.

## REFERENCES

(1) Lu, M.-P.; Song, J.; Lu, M.-Y.; Chen, M.-T.; Gao, Y.; Chen, L.-J.; Wang, Z. L. Piezoelectric nanogenerator using p-type ZnO nanowire arrays. *Nano Lett.* **2009**, *9*, 1223−1227.

(2) Kwon, J.; Seung, W.; Sharma, B. K.; Kim, S.-W.; Ahn, J.-H. A high performance PZT ribbon-based nanogenerator using graphene transparent electrodes. *Energy Environ. Sci.* **2012**, *5*, 8970−8975.

(3) Kumar, C.; Gaur, A.; Rai, S. K.; Maiti, P. Piezo devices using poly (vinylidene fluoride)/reduced graphene oxide hybrid for energy harvesting. *Nano-Struct. Nano-Objects* **2017**, *12*, 174−181.

(4) Araneo, R.; Falconi, C. Lateral bending of tapered piezo-semiconductive nanostructures for ultra-sensitive mechanical force to voltage conversion. *Nanotechnology* **2013**, *24*, No. 265707.

(5) Wu, W.; Pan, C.; Zhang, Y.; Wen, X.; Wang, Z. L. Piezotronics and piezo-phototronics − from single nanodevices to array of devices and then to integrated functional system. *Nano Today* **2013**, *8*, 619.

(6) Ismailzade, I. H.; Alecberov, A. I.; Ismailov, R. M.; Aliyez, I. M.; Rzayev, D. A. A new ferroelectric-semiconductor $V_2O_5$. *Ferroelectrics* **1980**, *23*, 47−50.

(7) Orgel, L. E. Ferroelectricity and the structure of transition-metal oxides. *Discuss. Faraday Soc.* **1958**, *26*, 138−144.

(8) Morin, F. J. Oxides which show a metal-to-insulator transition at the Neel temperature. *Phys. Rev. Lett.* **1959**, *3*, 34.

(9) Haverkort, M. W.; Hu, Z.; Tanaka, A.; Reichelt, W.; Streltsov, S. V.; Korotin, M. A.; Anisimov, V. I.; Hsieh, H. H.; Lin, H. -J.; Chen, C. T.; Khomskii, D. I.; Tjeng, L. H. Orbital-assisted metal-insulator transition in $VO_2$. *Phys. Rev. Lett.* **2005**, *95*, No. 196404.

(10) Kim, H. -T.; Lee, Y. W.; Kim, B. -J.; Chae, B. -G.; Yun, S. J.; Kang, K. -Y.; Han, K. -J.; Yee, K. -J.; Lim, Y. -S. Monoclinic and correlated metal phase in $VO_2$ as evidence of the Mott transition: coherent phonon analysis. *Phys. Rev. Lett.* **2006**, *97*, No. 266401.

(11) Zylbersztejn, A.; Mott, N. F. Metal-insulator transition in vanadium dioxide. *Phys. Rev. B* **1975**, *11*, 4383.

(12) Marezio, M.; Dernier, P. D.; Santoro, A. Twinning in Cr-doped VO$_2$. *Acta Crystallogr., Sect. A: Cryst. Phys., Diffr., Theor. Gen. Crystallogr.* **1973**, *29*, 618.

(13) Cavalleri, A.; Dekorsy, T.; Chong, H. H. W.; Kieffer, J. C.; Schoenlein, R. W. Evidence for a structurally-driven insulator-to-metal transition in VO$_2$: A view from the ultrafast timescale. *Phys. Rev. B* **2004**, *70*, No. 161102.

(14) Goodenough, J. B. The two components of the crystallographic transition in VO$_2$. *J. Solid State Chem.* **1971**, *3*, 490−500.

(15) Strelcov, E.; Tselev, A.; Ivanov, I.; Budai, J. D.; Zhang, J.; Tischler, J. Z.; Kravchenko, I.; Kalinin, S. V.; Kolmakov, A. Doping-based stabilization of the M2 phase in free-standing VO$_2$ nanostructures at room temperature. *Nano Lett.* **2012**, *12*, 6198−6205.

(16) Eyert, V. The Metal-insulator transitions of VO$_2$: A band theoretical approach. *Ann. Phys.* **2002**, *11*, 650−702.

(17) Pouget, J. P.; Launois, H.; D'Haenens, J. P.; Merenda, P.; Rice, T. M. Electron localization induced by uniaxial stress in pure VO$_2$. *Phys. Rev. Lett.* **1975**, *35*, 873−875.

(18) Yang, Z.; Ko, C.; Balakrishnan, V.; Gopalakrishnan, G.; Ramanathan, S. Dielectric and carrier transport properties of vanadium dioxide thin films across the phase transition utilizing gated capacitor devices. *Phys. Rev. B* **2010**, *82*, No. 205101.

(19) Park, J. H.; Coy, J. M.; Kasirga, T. S.; Huang, C.; Fei, Z.; Hunter, S.; Cobden, D. H. Measurement of a solid-state triple point at the metal-insulator transition in VO$_2$. *Nature* **2013**, *500*, 431−434.

(20) Kikuzuki, T.; Lippmaa, M. Characterizing a strain-driven phase transition in VO$_2$. *Appl. Phys. Lett.* **2010**, *96*, No. 132107.

(21) Hammersley, A. P. *FIT2D: An Introduction and Overview*; ESRF Internal Report, ESRF97HA02T 1997.

(22) Toby, B. H. EXPGUI, a graphical user interface for GSAS. *J. Appl. Crystallogr.* **2001**, *34*, 210−213.

(23) Momma, K.; Izumi, F. VESTA: a three-dimensional visualization system for electronic and structural analysis. *J. Appl. Crystallogr.* **2008**, *41*, 653−658.

(24) Basu, R.; Patsha, A.; Chandra, S.; Amirthapandian, S.; Raghavendra, K. G.; Dasgupta, A.; Dhara, S. Polarized Raman scattering study confirming the observation of spinon-vibration in VO$_2$. *J. Phys. Chem. C* **2019**, *123*, 11189.

(25) Goodenough, J. B.; Hong, H. Y. Structures and a two-band model for the system V$_{1−x}$Cr$_x$O$_2$. *Phys. Rev. B* **1973**, *8*, 1323.

(26) Marezio, M.; McWhan, D. B.; Remeika, J. P.; Dernier, P. D. Structural aspects of the metal-insulator transitions in Cr-Doped VO$_2$. *Phys. Rev. B* **1972**, *5*, 2541.

(27) Mitsuishi, T. On the Phase Transformation of VO$_2$. *Jpn. J. Appl. Phys.* **1967**, *6*, 1060.

(28) Basu, R.; Dhara, S. Polarized Raman scattering study confirming the observation of spinon-vibration in VO$_2$. *AIP Conf. Proc.* **2020**, *2265*, No. 030011.

(29) Basu, R.; Srihari, V.; Sardar, M.; Srivastava, S. K.; Bera, S.; Dhara, S. Probing phase transition in VO$_2$ with the novel observation of low-frequency collective spin excitation. *Sci. Rep.* **2020**, *10*, No. 1977.

(30) Heckingbottom, R.; Linett, J. W. Structure of vanadium dioxide. *Nature* **1962**, *194*, 678.

(31) Kim, H.-T.; et al. Raman study of electric-field-induced first-order metal-insulator transition in VO$_2$-based devices. *Appl. Phys. Lett.* **2005**, *86*, No. 242101.

(32) Marini, C.; Arcangeletti, E.; Castro, D. D.; Baldassare, L.; Perucchi, A.; Lupi, S.; Malavasi, L.; Boeri, L.; Pomjakushina, E.; Conder, K.; Postorino, P. Optical properties of V$_{1−x}$Cr$_x$O$_2$ compounds under high pressure. *Phys. Rev. B* **2008**, *77*, No. 235111.

(33) Chen, X.-B. Assignment of the Raman modes of VO$_2$ in the monoclinic insulating phase. *J. Korean Phys. Soc.* **2011**, *58*, 100−104.

(34) Srivastava, R.; Chase, L. Raman Spectrum of Semiconducting and Metallic VO$_2$. *Phys. Rev. Lett.* **1971**, *27*, 727.

(35) Vikhnin, V.; Goncharuk, I.; Davydov, V. Y.; Chudnovskii, F.; Shadrin, E. Raman light scattering of vanadium dioxide high-temperature phase and the model of structural transformations near

metal-semiconductor phase transition. *Fiz. Tverd. Tela* **1995**, *37*, 3580−3596.

(36) Basu, R.; Sardar, M.; Bera, S.; Magudapathy, P.; Dhara, S. The role of 1-d finite size Heisenberg chains in increasing the metal to insulator transition temperature in hole rich VO$_2$. *Nanoscale* **2017**, *9*, 6537.

(37) Chen, C.; Fan, Z. Changes in VO$_2$ band structure induced by charge localization and surface segregation. *Appl. Phys. Lett.* **2009**, *95*, No. 262106.

(38) Miao, P.; Zhao, Y.; Luo, N.; et al. Ferroelectricity and self-polarization in ultrathin relaxor ferroelectric films. *Sci. Rep.* **2016**, *6*, No. 19965.

(39) Gruverman, A.; Kalinin, S. V. Piezoresponse force microscopy and recent advances in nanoscale studies of ferroelectrics. *J. Mater. Sci.* **2006**, *41*, 107−116.

(40) Zhao, M.-H.; Wang, Z.-L.; Mao, S. X. Piezoelectric characterization of individual zinc oxide nanobelt probed by piezoresponse force microscope. *Nano Lett.* **2004**, *4*, 587−590.

(41) Lu, M.-Y.; Song, J.; Lu, M.-P.; Lee, C.-Y.; Chen, L.-J.; Wang, Z. L. ZnO−ZnS heterojunction and ZnS nanowire arrays for electricity generation. *ACS Nano* **2009**, *3*, 357−362.

(42) Parida, S.; Mangamma, G.; Singha, C.; Bhattacharyya, A.; Dhara, S. Determining the polarity of droplet epitaxy grown AlGaN nanorods using piezoresponse force microscopy. *Nano-Struct. Nano-Objects* **2019**, *20*, No. 100398.

(43) Ku, N.-J.; Huang, J.-H.; Wang, C.-H.; Fang, H.-C.; Liu, C.-P. Crystal face-dependent nanopiezotronics of an obliquely aligned InN nanorod array. *Nano Lett.* **2012**, *12*, 562−568.

(44) Ku, N.-J.; Wang, C.-H.; Huang, J.-H.; Fang, H.-C.; Huang, P.-C.; Liu, C.-P. Energy harvesting from the obliquely aligned InN nanowire array with a surface electron-accumulation layer. *Adv. Mater.* **2013**, *25*, 861−866.